Long-wavelength equation for vertically falling films

Mohan K. R. Panga, Ramesh R. Mudunuri, and Vemuri Balakotaiah*
Department of Chemical Engineering, University of Houston, Houston, Texas 77204-4792, USA
(Received 24 April 2003; revised manuscript received 3 August 2004; published 22 March 2005)

An equation is derived for describing wave evolution on the surface of a vertically falling viscous film. The traditional long-wavelength scaling is replaced by a new scaling to reduce the two dimensional Navier-Stokes equations to a single evolution equation for the scaled film thickness $h(x,t)$. The scaling suggests that the Weber number (We) must be used instead of the Reynolds number (Re) to distinguish between viscous and inertia dominated regimes for vertically falling films. This equation includes viscous dissipation and pressure correction terms that are missing in the existing single evolution equations at the same order. Comparison of the neutral stability curves and growth rates predicted by different models to that of the Orr-Sommerfeld (OS) equation shows that our equation matches with the OS results better than the existing single evolution equations. However, our equation is not free from finite time blowup. Selective regularization leads to a two mode model in flow rate and film thickness. The regularized equation is free from finite time blowup and predicts two families of solitary waves. Numerical simulations of the derived equation and its regularized version in the traveling wave coordinate show the transition of wave structure from regular (periodic) to chaotic profiles. Model predictions on maximum wave amplitude on the low celerity branch show good agreement with experimental data.

DOI: 10.1103/PhysRevE.71.036310 PACS number(s): 47.20.−k, 05.45.−a, 47.20.Ma, 47.20.Ky

I. INTRODUCTION

Wave formation on vertically falling films has been investigated extensively in the last half century since the early work of Nusselt [1] and Kapitza and Kapitza [2]. Benjamin [3] showed that film flow down a vertical wall is unstable at all Reynolds numbers (Re). Surface waves which arise as a result of this instability are observed to show a complex and rich spectrum of behavior [4,5]. It is now well established both experimentally and theoretically that these waves exhibit spatiotemporal chaos at any $\mathrm{Re}>0$. A major unsettled question is whether there exists a low-dimensional model that can describe the wave amplitudes observed in the experiments qualitatively and quantitatively.

One of the approaches used to derive low-dimensional models is the long-wavelength type perturbation expansion which gives a single evolution equation for the film thickness. For example, for the case of two dimensional Navier-Stokes (NS) equations, we have the well known long-wavelength equation derived by Benney [6]:

$$\frac{\partial h}{\partial t}+3h^2h_x+\frac{\partial}{\partial x}\left[\frac{3}{10}\mathrm{Re}\,h^6h_x+\frac{\mathrm{Re\,We}}{12}h^3h_{xxx}\right]=0, \quad (1)$$

where h is the scaled film thickness, Re is the film Reynolds number, and We is the Weber number. A weakly nonlinear truncation (i.e., expanding around $\mathrm{Re}=0$, $\eta=h-1=0$, and keeping only linear and quadratic terms) of the long-wavelength equation gives the widely studied Kuramoto-Sivashinsky equation (after scaling x, t, and η):

$$\eta_T+\eta\eta_X+\eta_{XX}+\eta_{XXXX}=0. \quad (2)$$

An alternate approach based on integral boundary layer techniques is also used to derive low-dimensional models for film flow. In this approach, the long-wavelength scaling is combined with an assumed velocity profile and the equations of motion are averaged in the direction perpendicular to the flow. A well known model derived using this approach is the Shkadov model:

$$\frac{\partial h}{\partial t}+\frac{\partial q}{\partial x}=0,$$

$$\frac{\partial q}{\partial t}+\frac{6}{5}\frac{\partial}{\partial x}\left(\frac{q^2}{h}\right)=\frac{12}{\mathrm{Re}}h-\frac{12}{\mathrm{Re}h^2}q+\mathrm{We}h\frac{\partial^3 h}{\partial x^3}, \quad (3)$$

where h is the film thickness and q is the local flow rate.

Recent experimental data [7] on wave amplitudes have shown that the above Eqs. (1)–(3) cannot describe the observed wave amplitudes. The main reason for this is attributed to the omission of some viscous dissipation terms. Though higher order long-wavelength expansions by Gjevik [8] and Nakaya [9] include viscous dissipation terms, it was shown recently [7] that they too cannot capture the film behavior quantitatively. Improved versions of the Shkadov model, known as the three equation models (for film thickness, flow rate, and wall shear stress), derived by Ruyer-Quil and Manneville [10] and Nguyen and Balakotaiah [7], can describe the wave amplitudes quantitatively and are simpler than the Navier-Stokes equations but they are not as appealing as the single equation models.

The main objective of the current work is to derive a low-dimensional model that can describe the wave amplitudes both qualitatively and quantitatively. Our approach for deriving the model equation is different from those in the

*Corresponding author. Email address: bala@uh.edu

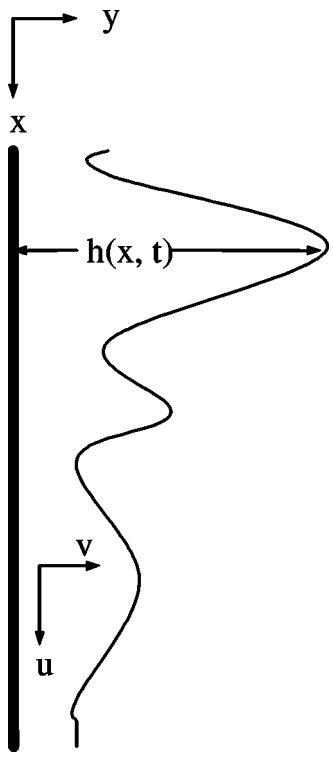

FIG. 1. Schematic diagram of film flow down a vertical wall.

literature and is detailed here. The new evolution equation also predicts qualitatively the recent experimental observations on wave suppression in viscous films at Weber numbers of order unity.

A summary of this model and its predictions are given in Panga and Balakotaiah [11]. In this paper, we present the derivation of the evolution equation along with its regularized form, bifurcation analysis of the model in the traveling wave coordinate, additional numerical results, and comparison with experimental data.

II. GOVERNING EQUATIONS

We consider the flow of a liquid film down a vertical wall under the action of gravity. The effects of the gas phase on the film are assumed to be negligible. This assumption is good as long as the gas phase is quiescent and its density and viscosity are negligible compared to the liquid phase. Figure 1 shows a schematic of the two dimensional flow. The coordinate axes are chosen such that the x axis points in the flow direction and the y axis in the direction perpendicular to the flow. The basic equations and boundary conditions describing the flow are given by the two dimensional Navier-Stokes equations (4)–(9):

$$\frac{D\mathbf{u}}{Dt'} = -\frac{1}{\rho}\nabla p' + \mathbf{g} + \nu\nabla^2\mathbf{u}, \tag{4}$$

$$\nabla \cdot \mathbf{u} = 0, \tag{5}$$

$$u' = v' = 0 \quad \text{at} \quad y' = 0, \tag{6}$$

$$v' = \frac{\partial h'}{\partial t'} + u'\frac{\partial h'}{\partial x'} \quad \text{at} \quad y' = h'(x',t'), \tag{7}$$

$$\left(\frac{\partial u'}{\partial y'} + \frac{\partial v'}{\partial x'}\right)(1 - h_{x'}'^2) + \left(\frac{\partial v'}{\partial y'} - \frac{\partial u'}{\partial x'}\right)(2h_{x'}') = 0 \quad \text{at} \quad y' = h'(x',t'), \tag{8}$$

$$p' - p_o' + 2\mu\left(\frac{\partial u'}{\partial y'} + \frac{\partial v'}{\partial x'}\right)\frac{h_{x'}'}{1 + h_{x'}'^2} + 2\mu\frac{\partial u'}{\partial x'}\frac{1 - h_{x'}^2}{1 + h_{x'}'^2} + \sigma\frac{h_{x'x'}'}{(1 + h_{x'}'^2)^{3/2}} = 0 \quad \text{at} \quad y' = h'(x',t'), \tag{9}$$

where $\mathbf{u} = (u', v')$ is the velocity vector, p' is the pressure, $h'(x',t')$ is the height of the film (measured from the wall), g is the acceleration due to gravity, μ is the viscosity, ν is the kinematic viscosity, σ is the surface tension, and p_o' is the pressure in the gas phase adjacent to the film. The prime denotes dimensional variables. The boundary conditions are given by Eq. (6)–(9). Equations (6) and (7) represent the no slip boundary condition at the wall and the kinematic boundary condition at the interface, respectively. The continuity of tangential and normal stresses at the interface is described by Eqs. (8) and (9), respectively.

One of the solutions to the above set of equations is the flat film solution (Nusselt's solution) obtained by balancing the viscous and gravitational forces. The velocity profile for the flat film solution is given by

$$u' = \frac{gh_N^2}{2\nu}\left[2\left(\frac{y'}{h_N}\right) - \left(\frac{y'}{h_N}\right)^2\right]. \tag{10}$$

We use Nusselt's flat film solution to define an average Nusselt velocity $u_N = gh_N^2/3v$. Equations (4)–(9) are made dimensionless by choosing average velocity u_N and flat film thickness h_N as characteristic velocity and length scales, respectively. The resulting dimensionless variables and dimensionless groups are shown below:

$$x = \frac{x'}{h_N}, \quad y = \frac{y'}{h_N}, \quad t = \frac{t'}{(h_N/u_N)},$$

$$u = \frac{u'}{u_N}, \quad v = \frac{v'}{u_N}, \quad p = \frac{p'}{\left(\frac{\mu u_N}{4h_N}\right)},$$

$$\mathrm{Re} = \frac{4u_N h_N}{\nu} = \frac{4gh_N^3}{3\nu^2}, \quad \mathrm{Ka} = \frac{\sigma\rho^{1/3}}{g^{1/3}\mu^{4/3}}.$$

The system has *two independent dimensionless groups*, the Reynolds number (Re) and the Kapitza number (Ka). Since the Kapitza number is only dependent on the fluid physical properties, it is constant for a given fluid. We also use the Weber number (We) which is related to Re and Ka as follows:

$$\mathrm{We} = \frac{\sigma}{\rho u_N^2 h_N} = \frac{9\sigma\mu^2}{\rho^3 g^2 h_N^5} = 3^{1/3}4^{5/3}\frac{\mathrm{Ka}}{\mathrm{Re}^{5/3}} = C\frac{\mathrm{Ka}}{\mathrm{Re}^{5/3}}, \quad (11)$$

where $C=3^{1/3}4^{5/3}$. The dimensionless equations are given by

$$\left(\frac{C\,\mathrm{Ka}}{\mathrm{We}}\right)^{3/5}\frac{Du}{Dt} = -\frac{\partial p}{\partial x} + 12 + 4\nabla^2 u, \quad (12)$$

$$\left(\frac{C\,\mathrm{Ka}}{\mathrm{We}}\right)^{3/5}\frac{Dv}{Dt} = -\frac{\partial p}{\partial y} + 4\nabla^2 v, \quad (13)$$

$$\frac{\partial u}{\partial x} + \frac{\partial v}{\partial y} = 0, \quad (14)$$

$$u = v = 0 \quad \text{at} \quad y = 0, \quad (15)$$

$$v = \frac{\partial h}{\partial t} + u\frac{\partial h}{\partial x} \quad \text{at} \quad y = h(x,t), \quad (16)$$

$$\left(\frac{\partial u}{\partial y} + \frac{\partial v}{\partial x}\right)(1 - h_x^2) + \left(\frac{\partial v}{\partial y} - \frac{\partial u}{\partial x}\right)(2h_x) = 0 \quad \text{at} \quad y = h(x,t), \quad (17)$$

$$p + 8\left(\frac{\partial u}{\partial y} + \frac{\partial v}{\partial x}\right)\frac{h_x}{1+h_x^2} + 8\frac{\partial u}{\partial x}\frac{1-h_x^2}{1+h_x^2} + (C\,\mathrm{Ka})^{3/5}\mathrm{We}^{2/5}\frac{h_{xx}}{(1+h_x^2)^{3/2}} = 0 \quad \text{at} \quad y = h(x,t). \quad (18)$$

III. SCALING

The two-dimensional Navier-stokes (NS) equations (12)–(18) are traditionally reduced to a single evolution equation using a perturbation expansion in terms of the wave number α, along with the assumptions $\mathrm{Re}\sim O(1)$ and $\alpha^2\,\mathrm{We}\sim O(1)$. For example, the equation for the case of large Weber number, $\alpha^2\,\mathrm{We}\sim O(1)$, truncated at $O(\alpha)$ gives the long-wavelength equation (LW)

$$\frac{\partial h}{\partial t} + 3h^2 h_x + \frac{\partial}{\partial x}\left[\frac{3}{10}\mathrm{Re}h^6 h_x + \frac{\mathrm{Re\ We}}{12}h^3 h_{xxx}\right] = 0. \quad (19)$$

We derive a single evolution equation using a long-wavelength expansion ($\alpha \ll 1$), for the case of large Weber number $\alpha^2\,\mathrm{We}\sim O(1)$. However, *unlike the long-wavelength scaling, we assume* $\mathrm{Ka}\sim O(1)$ *and do not impose any direct restriction on the Reynolds number*. The resulting equation truncated at $O(\alpha^{2.2})$ is given by

$$\frac{\partial h}{\partial t} + 3h^2 h_x + \frac{\partial}{\partial x}\left[3h^4 h_{xx} + 7h^3 h_x^2 - \frac{5}{32}\mathrm{Re}h^4 h_t - \frac{27}{160}\mathrm{Re}h^6 h_x + \frac{\mathrm{Re\ We}}{12}h^3 h_{xxx}\right] = 0. \quad (20)$$

An interesting feature of Eq. (20) is that it has viscous dissipation and pressure correction terms, $3h^4 h_{xx}$ and $7h^3 h_x^2$, which are missing in the LW equation (19). We find that these terms are essential to capture the qualitative behavior of wave evolution and hence are required for describing waves on viscous films quantitatively. In addition, replacing the time derivative by the spatial derivative in the term $-5/32\mathrm{Re}h^4 h_t$, as done in the LW equation (19), leads to nonphysical wave celerities and poor quantitative agreement with experimental data. The difference between our scaling and the traditional long-wavelength scaling is discussed in the remaining part of this section.

Long-wavelength scaling parameter $\alpha(=2\pi h_N/\lambda)$ is introduced into the system (12)–(18) by scaling the length in the flow direction with $\lambda/2\pi$ where λ is an unknown wavelength. The wave number α is assumed to be small. The NS equations are then reduced to a single evolution equation by an asymptotic expansion in α along with the long-wavelength scaling $\mathrm{Re}\sim O(1)$ and $\alpha^2\,\mathrm{We}\sim O(1)$. The validity of the assumption, α being small, depends on the magnitude of the parameters Re and We [15]. For large Weber numbers, this is a reasonable assumption because the waves on the surface of a falling film are observed to have long wavelengths compared to the thickness of the film for $\mathrm{We} \gg 1$ [18]. Assuming α is small, the long-wavelength expansion when truncated at $O(\alpha)$ gives the long-wavelength equation (19). At the lowest order in the expansion, viscous and gravitational forces balance each other and corrections to the lowest order solution come from the inertial and capillary terms. Notice that, in this procedure, irrespective of the magnitude of the viscous and inertial forces in the film, the correction to the lowest order solution always comes from inertial terms. Viscous terms, which play an important role in governing the dynamics of the small amplitude waves and thin films are missing in the correction to the lowest order solution in the long-wavelength expansion. Because of these missing terms, the long-wavelength equation does not predict wave dispersion and overpredicts the critical wave numbers as compared to those predicted by the Orr-Sommerfeld equations obtained by linearizing NS equations. To include the viscous terms, long-wavelength expansion is carried to higher orders [8,9]. These higher order approximations bring in the viscous terms but they contain more inertial terms (such as Re^2, Re^3, etc.) than the dissipative terms and therefore the imbalance between inertial and viscous effects present at lower orders persists at higher orders. Hence carrying the expansion to a higher order fails [7] to rectify the problem.

Intuitively, the terms that correct the lowest order solution depend on the relative importance of viscous, inertial, and capillary forces in the film. Traditionally, the Reynolds number is used to differentiate between viscous and inertia dominated regimes (e.g., flow in a pipe). For falling films, the velocity and film thickness used in the definition of Reynolds number are not independent of each other and hence, the Reynolds number (Re) alone is not sufficient to distinguish between inertia and viscous dominated regimes. This leads to the question whether there is a parameter whose magnitude is indicative of the relative importance of the inertial terms compared to viscous and/or capillary terms. If such a parameter exists, then its magnitude would allow us to determine

the terms that correct the lowest order solution. Here, we argue that the Weber number plays such a role. Irrespective of the Kapitza number or the fluid, a large Weber number $(1/\mathrm{We}\rightarrow 0)$ implies that viscous or capillary effects are dominant in the film compared to the inertial effects and a small Weber number $(\mathrm{We}\rightarrow 0)$ represents strong inertial effects. For example, let us consider two fluids one being water and the other a 95% gylcerin solution. The Kapitza numbers for these fluids are 3371 and 0.24, respectively. For Reynolds number of unity $(\mathrm{Re}=1)$ the Weber numbers for these fluids are 48 980 and 3.48, respectively. The thickness of the water film for $\mathrm{Re}=1$ is 0.0425 mm while for glycerin solution it is 4.25 mm. When compared to the water film at the same Reynolds number, the glycerin film has a thickness which is hundred times larger than that of water. While viscous forces are dominant in the thin water film for $\mathrm{Re}=1$, inertial forces may also become important in the glycerin film which is thick at the same Reynolds number $(\mathrm{Re}=1)$. The above comparison shows that for the same Reynolds number, either viscous or both viscous and inertial forces can become important depending on the Kapitza number. Hence the magnitude of the Reynolds number is not indicative of viscous or inertia dominated regimes, whereas for the water film where viscous effects are dominant, the Weber number is large and for the glycerin film where viscous and inertial effects may be of equal order, the Weber number is of order unity. Unlike the Reynolds number, a large Weber number implies viscous dominated regime and a small Weber number represents the inertia dominated regime for falling films. Thus the correction to the lowest order solution depends on the Weber number, not on the Reynolds number.

We replace the assumption of $\mathrm{Re}\sim O(1)$ by $\mathrm{Ka}\sim O(1)$ in the long-wavelength scaling and retain the large Weber number assumption $\alpha^2\,\mathrm{We}\sim O(1)$, to derive a single evolution equation. Rearranging the relation between We, Ka, and Re [Eq. (11)] and using the scaling $\mathrm{Ka}\sim O(1)$ and $\alpha^2\,\mathrm{We}=\mathrm{W}\sim O(1)$ we get

$$\mathrm{Re}=(C\,\mathrm{Ka})^{3/5}\left(\frac{1}{\mathrm{We}}\right)^{3/5}=\left(\frac{C\,\mathrm{Ka}}{W}\right)^{3/5}\alpha^{6/5}=\beta\alpha^{6/5}, \quad (21)$$

where $\beta=(C\,\mathrm{Ka}/\mathrm{W})^{3/5}$ is an $O(1)$ parameter. The scaling $\mathrm{Re}=\beta\alpha^{6/5}$ suggests that viscous effects should be given more importance than inertial effects while deriving evolution equations for large Weber numbers $(\mathrm{We}\gg 1)$. Viscous and inertial effects are of equal order when $\mathrm{We}\sim O(1)$. Inertial effects are dominant in the film for $\mathrm{We}\ll 1$. The large Weber number limit $(\mathrm{We}\gg 1)$ where viscous or capillary effects are strong is referred to as the *viscocapillary* regime [12]. In terms of the Reynolds number, the viscocapillary regime corresponds to $0<\mathrm{Re}\ll 4^{*}3^{1/5}\mathrm{Ka}^{3/5}(\approx 5\,\mathrm{Ka}^{3/5})$. The range of Reynolds numbers which define the viscocapillary regime depends on the Kapitza number. For Reynolds numbers outside this range, inertial effects become important. Thus for small Ka numbers inertial effects can become important at low Reynolds numbers. Taking $\mathrm{We}=1$ as the cutoff point, the viscocapillary regime for water $(\mathrm{Ka}=3371)$ corresponds to $0<\mathrm{Re}\ll 650$, while for 95% glycerin solution $(\mathrm{Ka}=0.24)$ it is defined by $0<\mathrm{Re}\ll 2.0$. In the example discussed before

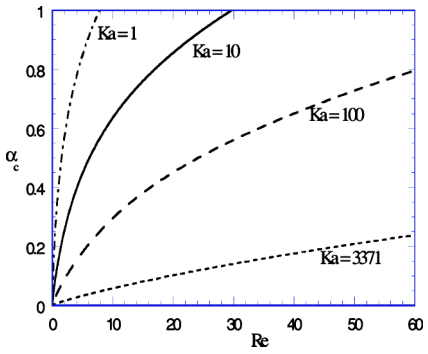

FIG. 2. Neutral stability curves obtained from Orr-Sommerfeld equations for different fluids.

for $\mathrm{Re}=1$, water is well within the viscocapillary regime, whereas glycerin falls on the boundary where viscous and inertial effects are of equal importance.

The advantages of using the scaling $\mathrm{Ka}\sim O(1)$ and $\alpha^2\,\mathrm{We}\sim O(1)$ instead of the long-wavelength scaling $\mathrm{Re}\sim O(1)$ and $\alpha^2\,\mathrm{We}\sim O(1)$ can be seen from linear stability results of the NS equations. Figure 2 shows the neutral stability curves obtained from the Orr-Sommerfeld equations for different fluids or Kapitza numbers. In this figure, the neutrally stable wave number is plotted against Re for different Ka numbers. However, when the same neutral curves are plotted with the reciprocal of Weber number (Fig. 3), it is interesting to notice that all the curves collapse onto a single curve for large Weber number $(1/\mathrm{We}\rightarrow 0)$ and tend to remain close up to Weber numbers of order unity. In these plots the Kapitza number is varied between 1 and 3371. Even for large variation in the Kapitza number, in the limit $1/\mathrm{We}\rightarrow 0$, the results are independent of Ka number as stated earlier, and weakly dependent on Ka for Weber numbers of order unity, whereas the neutral stability curves remain distinct when plotted with Reynolds number even in the limit $\mathrm{Re}\rightarrow 0$. Another observation to be made from Fig. 3 is that the critical wavelength α_c remains small as long as the Weber number is large irrespective of the Kapitza number. Thus the long-wavelength assumption $\alpha\ll 1$ is valid for large Weber number, $\alpha^2\,\mathrm{We}\sim O(1)$.

In the next section, we discuss the perturbation expansion with the new scaling $\mathrm{Ka}\sim O(1)$ and $\alpha^2\,\mathrm{We}\sim O(1)$. The expansion, unlike the traditional long-wavelength expansion, corrects the lowest order solution with viscous and pressure

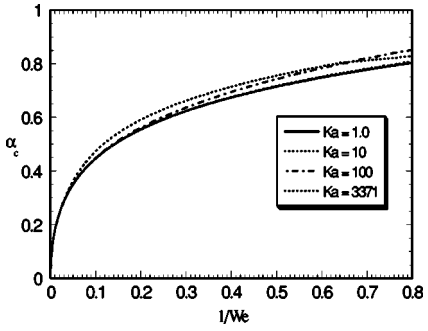

FIG. 3. Neutral stability curves in Fig. 2 are plotted with the reciprocal of Weber number.

terms in the viscocapillary regime. A major improvement in our model derived using this scaling is that it restores a balance between inertial and viscous effects at the lowest order.

IV. PERTURBATION EXPANSION

We introduce the scaling $\mathrm{Ka} \sim O(1)$ and $\alpha^2\,\mathrm{We} = \mathrm{W} \sim O(1)$ into the dimensionless equations (12)–(18). The new dimensionless coordinates (X, Y, τ) and variables (U, V, P) expressed in terms of the old dimensionless coordinates and variables are shown below:

$$X = \alpha x, \quad Y = y, \quad \tau = \alpha t,$$

$$u = U, \quad v = \alpha V, \quad p = P.$$

Since the resulting system of equations after introducing the scaling contains fractional powers of α, a new parameter γ is used in place of α to eliminate the fractional powers. The relationship between the parameters γ and α, and the scaling in terms of γ is shown in Eqs. (22)–(24):

$$\gamma = \alpha^{1/5}, \tag{22}$$

$$\alpha = \gamma^5, \quad \gamma^{10}\,\mathrm{We} = W \sim O(1), \tag{23}$$

$$\left(\frac{C\,\mathrm{Ka}}{\mathrm{We}}\right)^{3/5} = \left(\frac{C\,\mathrm{Ka}}{W}\right)^{3/5} \alpha^{6/5} = \beta\gamma^6, \tag{24}$$

where $\beta = (C\,\mathrm{Ka}/W)^{3/5} \sim O(1)$. The scaled equations are given by

$$\beta\gamma^{11}(U_\tau + UU_X + VU_Y) = -\gamma^5 P_X + 12 + 4(U_{YY} + \gamma^{10}U_{XX}), \tag{25}$$

$$\beta\gamma^{16}(V_\tau + UV_X + VV_Y) = -P_Y + 4(\gamma^5 V_{YY} + \gamma^{15}V_{XX}), \tag{26}$$

$$U_X + V_Y = 0, \tag{27}$$

$$U = V = 0, \quad \text{for} \quad Y = 0, \tag{28}$$

$$V = h_\tau + Uh_X \quad \text{for} \quad Y = h(X,\tau), \tag{29}$$

$$(U_Y + \gamma^{10}V_X)(1 - \gamma^{10}h_X^2) + (V_Y - U_X)(2\gamma^{10}h_X) = 0 \quad \text{for} \quad Y = h(X,\tau), \tag{30}$$

$$P + 8\gamma^5(U_Y + \gamma^{10}V_X)\frac{h_X}{1 + \gamma^{10}h_X^2} + 8\gamma^5 U_X\frac{1 - \gamma^{10}h_X^2}{1 + \gamma^{10}h_X^2} + \beta W\gamma^6\frac{h_{XX}}{(1 + \gamma^{10}h_x^2)^{3/2}} = 0 \quad \text{for} \quad Y = h(X,\tau). \tag{31}$$

Due to the way the perturbation parameter γ appears in the scaled equations, corrections to the lowest order $O(\gamma^o)$ are only made at $O(\gamma^5)$, $O(\gamma^6)$, $O(\gamma^{10})$, $O(\gamma^{11})$, $O(\gamma^{15})$, $O(\gamma^{16})$, and so on. The lowest order $O(\gamma^o)$ equations are given by

$$12 + 4\frac{\partial^2 U_o}{\partial Y^2} = 0, \quad -\frac{\partial P_o}{\partial Y} = 0, \quad \frac{\partial U_o}{\partial X} + \frac{\partial V_o}{\partial Y} = 0, \tag{32}$$

$$\left.\frac{\partial U_o}{\partial Y}\right|_{Y=h} = 0, \quad P_o|_{Y=h} = 0, \quad U_o|_{Y=o} = V_o|_{Y=o} = 0. \tag{33}$$

The solution to this set of equations is

$$U_o = -\frac{3Y^2}{2} + 3hY, \quad V_o = -\frac{3h_X Y^2}{2}, \quad P_o = 0. \tag{34}$$

The evolution equation (35) at this order is obtained by substituting the velocities in the kinematic boundary condition. This equation is the same as obtained by simple long-wavelength scaling at the lowest order:

$$\frac{\partial h}{\partial \tau} + 3h^2 h_X = 0. \tag{35}$$

The above equation describes the evolution of waves with infinitely long wavelengths. When the wavelength becomes finite, the expansion should be carried to higher orders. Equations (36) and (37) show the corrections to velocity and pressure at $O(\gamma^5)$ and $O(\gamma^6)$, respectively.

$$U_5 = V_5 = 0, \quad P_5 = -12h_X Y - 12hh_X, \tag{36}$$

$$U_6 = V_6 = 0, \quad P_6 = -\beta W h_{XX}. \tag{37}$$

Only pressure is corrected at these orders. Since there is no correction to the velocities, the evolution equation remains the same as Eq. (35). However, it should be observed that pressure gets corrected first, unlike the long-wavelength expansion where pressure correction is pushed to higher orders. The equations at $O(\gamma^{10})$ are given by

$$\frac{\partial^2 U_{10}}{\partial Y^2} = \frac{1}{4}\frac{\partial P_5}{\partial X} - \frac{\partial^2 U_o}{\partial X^2},$$

$$\frac{\partial P_{10}}{\partial Y} = 0,$$

$$\frac{\partial U_{10}}{\partial X} + \frac{\partial V_{10}}{\partial Y} = 0,$$

$$U_{10}|_{Y=0} = V_{10}|_{Y=0} = 0, \quad P_{10}|_{Y=h} = 0,$$

$$\left(\frac{\partial U_{10}}{\partial Y} + \frac{\partial V_o}{\partial X}\right) + \left(\frac{\partial V_o}{\partial Y} - \frac{\partial U_o}{\partial X}\right)(2h_X) = 0 \quad \text{at} \quad Y = h(X,\tau). \tag{38}$$

Notice that at this order the corrections to the velocity come from the viscous and pressure terms, whereas the correction to the lowest order comes from the inertial terms in the traditional long-wavelength expansion. Equations (38) include viscous terms in both the *x*-momentum equation and the tangential stress boundary condition. The evolution equation at $O(\gamma^{10})$ is given by Eq. (39):

$$\frac{\partial h}{\partial \tau} + 3h^2 h_X + \gamma^{10}\frac{\partial}{\partial X}[3h^4 h_{XX} + 7h^3 h_X^2] = 0. \tag{39}$$

The governing equations at $O(\gamma^{11})$ are given by

$$\frac{\partial^2 U_{11}}{\partial Y^2} = \frac{\beta}{4}\left(\frac{\partial U_o}{\partial \tau} + U_o\frac{\partial U_o}{\partial X} + V_o\frac{\partial U_o}{\partial Y}\right) + \frac{1}{4}\frac{\partial P_6}{\partial X},$$

$$\frac{\partial P_{11}}{\partial Y} = 0,$$

$$\frac{\partial U_{11}}{\partial X} + \frac{\partial V_{11}}{\partial Y} = 0,$$

$$U_{11}|_{Y=0} = V_{11}|_{Y=0} = 0, \quad P_{11}|_{Y=h} = 0,$$

$$\frac{\partial U_{11}}{\partial Y}|_{Y=h} = 0. \tag{40}$$

From the governing equations at $O(\gamma^{11})$, it can be seen that inertial and surface tension terms (in the form of pressure correction) affect the solution and the evolution equation at this order is given by

$$\frac{\partial h}{\partial \tau} + 3h^2 h_X + \gamma^{10}\frac{\partial}{\partial X}[3h^4 h_{XX} + 7h^3 h_X^2] + \gamma^{11}\frac{\partial}{\partial X}\left[-\frac{5}{32}\beta h^4 h_\tau - \frac{27}{160}\beta h^6 h_X + \frac{1}{12}\beta W h^3 h_{XXX}\right] = 0. \tag{41}$$

In terms of the wave number,

$$\left[\frac{\partial h}{\partial \tau} + 3h^2 h_X\right] + \alpha^2\frac{\partial}{\partial X}[3h^4 h_{XX} + 7h^3 h_X^2] + \alpha^{2.2}\frac{\partial}{\partial X} \times \left[-\frac{5}{32}\beta h^4 h_\tau - \frac{27}{160}\beta h^6 h_X + \frac{1}{12}\beta W h^3 h_{XXX}\right] = 0, \tag{42}$$

where we have grouped terms of the same order. If the perturbation expansion is carried in terms of α instead of γ, the correction to the evolution equation is made at orders α^2, $\alpha^{11/5}$, α^4, $\alpha^{21/5}$, $\alpha^{22/5}$, and so on. We truncate the perturbation expansion at $O(\alpha^{11/5})$ or $O(\gamma^{11})$ since it has all three viscous, inertial, and pressure corrections included in it. Removing the scaling from Eq. (42) , the evolution equation can be written in the old dimensionless variables as

$$\frac{\partial h}{\partial t} + 3h^2 h_x + \frac{\partial}{\partial x}\left[3h^4 h_{xx} + 7h^3 h_x^2 - \frac{5}{32}\mathrm{Re}h^4 h_t - \frac{27}{160}\mathrm{Re}h^6 h_x + \frac{\mathrm{Re\ We}}{12}h^3 h_{xxx}\right] = 0. \tag{43}$$

Evolution equation at the next order can be obtained by truncating the equation at $O(\alpha^{22/5})$. In case of inclined films, an additional term, $-\partial/\partial x(\cot\theta h^3 h_x)$ appears in the left-hand side of Eq. (43), where θ is the angle of inclination with the horizontal.

Exchange of time and spatial derivative

Equation (43) can be further simplified by replacing the time derivative in the term $\frac{5}{32}\mathrm{Re}h^4 h_t$ with a spatial derivative. Since $\frac{5}{32}\mathrm{Re}h^4 h_t$ is an $O(\gamma^{11})$ term, the time derivative term is replaced by its zeroth order approximation,

$$h_t = -3h^2 h_x + O(\gamma^{10}).$$

The terms of $O(\gamma^{21})$ are neglected. The evolution equation obtained after exchanging the time derivative with a spatial derivative is given by

$$h_t + 3h^2 h_x + \frac{\partial}{\partial x}\left[3h^4 h_{xx} + 7h^3 h_x^2 + \frac{3}{10}\mathrm{Re}h^6 h_x + \frac{\mathrm{Re\ We}}{12}h^3 h_{xxx}\right] = 0. \tag{44}$$

A similar exchange of time derivative with the spatial derivative in the expansion using traditional long-wavelength scaling gives LW equation (19). While this approximation is good for $\gamma \to 0$ or $1/\mathrm{We} \to 0$, we observe that for large but finite Weber numbers the predictions of Eq. (44) are both qualitatively and quantitatively different from those of Eq. (43). Comparing the maximum wave amplitudes obtained from the two equations (43) and (44) to experimental data shows that Eq. (43) describes the wave evolution on viscous films more accurately and retains the qualitative features of the Navier-Stokes equations up to Weber numbers of order unity. Benjamin *et al.* [13] made similar observations with the Korteweg-de Vries (KdV) equation. When the spatial derivative in the KdV equation was replaced by time derivative, the equation was found to have better properties.

V. COMPARISON OF EVOLUTION EQUATIONS

In this section, we compare our equation (43) with some of the existing evolution equations. When compared to the long-wavelength equation,

$$\frac{\partial h}{\partial t} + 3h^2 h_x + \alpha\frac{\partial}{\partial x}\left[\frac{3}{10}\mathrm{Re}h^6 h_x + \frac{\mathrm{Re\ We}}{12}h^3 h_{xxx}\right] = 0,$$

it can be seen that in our scaling there are no terms of order α and the viscous dissipation terms appear at order α^2 while the inertial and surface tension terms appear at order $\alpha^{2.2}$. In the long-wavelength scaling, the viscous and pressure correction terms are missing (at order α) while the inertial and surface tension terms appear at order α. Moreover, the mixed derivative in space and time is replaced with the spatial derivative in the long-wavelength equation.

Frenkel and Indireshkumar [14] derived an evolution equation based on minimal requirement of derivability (MRD) principle. Their equation obtained by combining the long-wavelength expansion with amplitude expansion is given by

$$\eta_t + 3\eta_x + 6\eta\eta_x + \frac{3}{10}\mathrm{Re}\,\eta_{xx} + \frac{\mathrm{Re\ We}}{12}\eta_{xxxx} + 3\eta_{xxx} = 0. \tag{45}$$

Comparing Eq. (45) to our equation in the weakly nonlinear form,

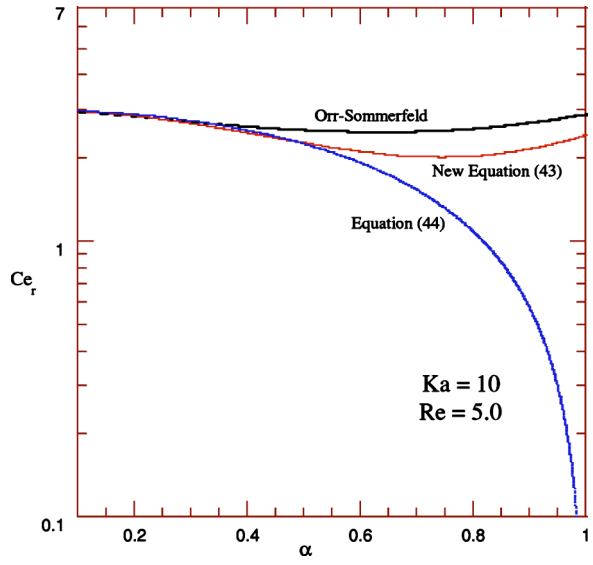

FIG. 4. Wave celerity (Ce_r) vs α for Ka=10.0 and Re=5.0.

$$\eta_t + 3\eta_x + 6\eta\eta_x + 3\eta_{xxx} - \frac{5}{32}\mathrm{Re}\,\eta_{xt} - \frac{27}{160}\mathrm{Re}\,\eta_{xx} + \frac{\mathrm{Re\ We}}{12}\eta_{xxxx} = 0, \tag{46}$$

it can be seen that the time derivative is exchanged with a spatial derivative in Eq. (45). The weakly nonlinear form of the evolution equations are only valid in the region where wave amplitudes are very small. Since the parameter region where wave amplitudes remain small is very narrow, the above equations are limited to a narrow region.

Ooshida [15] developed a regularized long-wavelength equation using Padé type approximation to increase the convergence boundaries of the long-wavelength equation. The regularized long-wavelength equation derived by Ooshida is given by

$$h_t - \frac{\partial}{\partial x}(h^2\partial_x\partial_t h) + \frac{\partial}{\partial x}\left[h^3 - \frac{5}{14}\mathrm{Re}h^4h_t - \frac{27}{35}\mathrm{Re}h^6h_x + \frac{\mathrm{ReWe}}{12}h^3h_{xxx}\right] = 0. \tag{47}$$

When compared to our equation, Ooshida's equation has an extra time derivative term and does not have the viscous and pressure correction terms ($3h^4h_{xx}$ and $7h^3h_x^2$) present in our equation. Interestingly, when the time derivative in the second term of Ooshida's equation is replaced with the approximation $h_t=-3h^2h_x$, Ooshida's equation reduces to the form of our new equation (43) with different numerical constants. The numerical constants are different because of the regularization procedure. The modified Ooshida's equation is given by

$$h_t + 3h^2h_x + \frac{\partial}{\partial x}\left[3h^4h_{xx} + 6h^3h_x^2 - \frac{5}{14}\mathrm{Re}h^4h_t - \frac{27}{35}\mathrm{Re}h^6h_x + \frac{\mathrm{Re\ We}}{12}h^3h_{xxx}\right] = 0. \tag{48}$$

Linear stability analysis of Ooshida's equation (47) shows that the regularization procedure overstabilizes the system. The reason for this overstabilization may be because of replacing the spatial derivative in the viscous and pressure correction terms with the time derivative. In the limit of We $\to\infty$, both the equations are similar, because the time derivative can be replaced by a spatial derivative and vice versa. However, for large but finite Weber numbers, use of time derivative instead of spatial derivative in the viscous and pressure correction terms introduces a stabilizing effect which is not present in the physical system. This will be shown using linear stability analysis in the next section.

VI. LINEAR STABILITY ANALYSIS

We verify the consistency and accuracy of our model by comparing the linear stability results of our Eq. (43) to that of Orr-Sommerfeld (OS) equation obtained by linearizing the Navier-Stokes equations around the flat film solution. Equation (43) when linearized around the Nusselts flat film solution $h=1$ gives

$$\eta_t + 3\eta_x + 3\eta_{xxx} - \frac{5}{32}\mathrm{Re}\,\eta_{tx} - \frac{27}{160}\mathrm{Re}\,\eta_{xx} + \frac{\mathrm{Re\ We}}{12}\eta_{xxxx} = 0, \tag{49}$$

where $\eta(x,t)$ is the deviation from the flat film thickness, $h(x,t)=1+\eta(x,t)$. We introduce sinusoidal perturbations (temporal formulation) of the form

$$\eta = \delta e^{i\alpha(x-\mathrm{Cet})} \tag{50}$$

into the linearized equation (49). Here δ is the wave amplitude, α is the wave number and $\mathrm{Ce}=\mathrm{Ce}_r+i\mathrm{Ce}_i$ is the celerity. The real part of celerity Ce_r gives the speed of the waves and imaginary part Ce_i gives the growth rate of the waves. The waves are unstable if the growth rate Ce_i is positive and vice versa. Substituting Eq. (50) into Eq. (49) yields the dispersion relation

$$-i\alpha\,\mathrm{Ce} + 3i\alpha - 3i\alpha^3 - \frac{5}{32}\mathrm{Re}\alpha^2\,\mathrm{Ce} + \frac{27}{160}\mathrm{Re}\alpha^2 + \frac{\mathrm{Re\ We}}{12}\alpha^4 = 0. \tag{51}$$

The wave celerity Ce_r and growth rate Ce_i could be obtained by separating the real and imaginary parts of the dispersion relation. The wave celerity and growth rate for different single evolution equations are given below.

Equation (43):

$$\mathrm{Ce}_r = \frac{3 + \left(\frac{135}{5120}\mathrm{Re}^2 - 3\right)\alpha^2 + \frac{5}{384}\mathrm{Re}^2\,\mathrm{We}\alpha^4}{1 + \frac{25}{1024}\mathrm{Re}^2\alpha^2}, \tag{52}$$

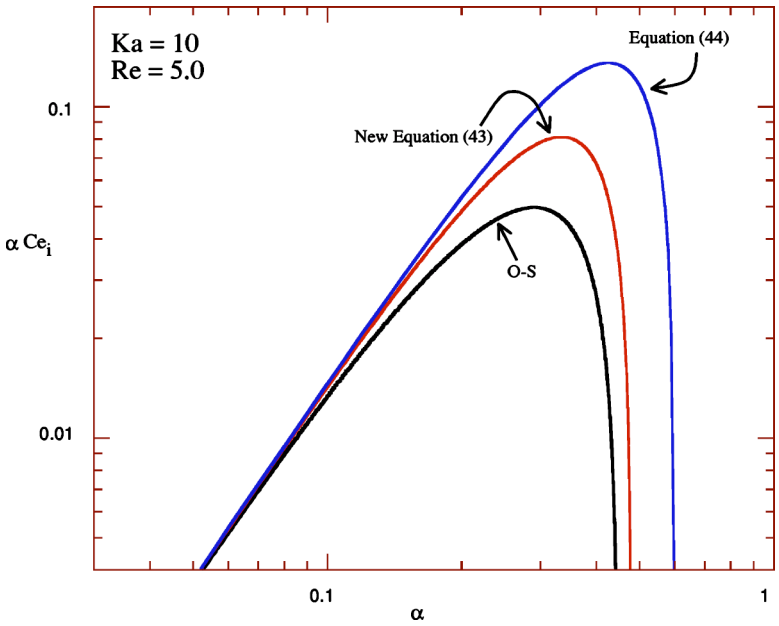

FIG. 5. Growth rate ($\alpha \mathrm{Ce}_i$) vs α for Ka $=10.0$ and Re$=5.0$.

$$\mathrm{Ce}_i = \frac{\frac{3}{10}\mathrm{Re}\alpha - \left(\frac{15}{32} + \frac{\mathrm{We}}{12}\right)\mathrm{Re}\alpha^3}{1 + \frac{25}{1024}\mathrm{Re}^2\alpha^2}. \tag{53}$$

Equation (44):

$$\mathrm{Ce}_r = 3(1 - \alpha^2), \tag{54}$$

$$\mathrm{Ce}_i = \frac{3}{10}\mathrm{Re}\alpha - \frac{\mathrm{Re\ We}}{12}\alpha^3. \tag{55}$$

Long-wavelength equation (19):

$$\mathrm{Ce}_r = 3,$$

$$\mathrm{Ce}_i = \frac{3}{10}\mathrm{Re}\alpha - \frac{\mathrm{Re\ We}}{12}\alpha^3.$$

Comparing the wave celerities obtained from the three equations, it could be seen that the wave speed predicted by Eqs. (44) and (19) are independent of the parameters Re and We, which is not the case in the real experiment. While the LW equation (19) shows no dispersion, i.e., all the wavelengths travel with equal velocity, the wave speeds predicted by Eq. (44) can become negative [Eq. (54)] for values of α greater than 1. This would lead to nonphysical upstream propagation of waves with wave numbers greater than 1. Both these problems are rectified in Eq. (43).

Comparison of model predictions with Orr-Sommerfeld results

Figures 4 and 5 show the wave celerities (Ce_r) and growth rates ($\alpha \mathrm{Ce}_i$) obtained from Eqs. (43) and (44), and OS as a function α for Ka$=10$ and Re$=5$. As mentioned earlier, the wave celerites and growth rates predicted by Eq. (43) are in better agreement with the OS than those of Eq. (44). Equation (44) predicts unusually large growth rates and amplifies even the shorter wavelengths. Hence the presence of short wavelengths or noise in the system is amplified when Eq. (44) is used to describe wave evolution though the short wavelengths are normally damped in the real system. Growth rate predictions of LW equation (19) are the same as Eq. (44).

The critical wave number (α_c) for neutrally stable waves is obtained by setting growth rate $\mathrm{Ce}_i = 0$ in Eq. (53):

$$\alpha_c = \left(\frac{3.6}{\frac{45}{8} + \mathrm{We}}\right)^{1/2}. \tag{56}$$

It follows from Eq. (56) that for We$\gg 1$ the neutral wave number approaches the limit (predicted by the long-wavelength as well as the OS equations)

$$\alpha_c = \sqrt{\frac{3.6}{\mathrm{We}}}.$$

However, for any finite value of We, α_c given by Eq. (56) never exceeds 0.8 while that predicted by the long-wavelength model is unbounded (as the Weber number, We $\ll 1$). Again, it is the viscous dissipation terms that arrest the growth of short wavelengths. Figure 6 shows the neutral stability curves of different models for Ka$=10$ as a function of the reciprocal of the Weber number. The region that lies below the neutral stability curve is unstable and the region above it is stable. A comparison of the evolution equations [LW, Nakaya, Ooshida equation (43), and its regularized version given by Eq. (77)] shows that the new equation (43) remains close to the OS in the viscocapillary regime. The long-wavelength and Nakaya models diverge from the OS within the viscocapillary regime. For very large Weber numbers, the new equation, Ooshida's equation and OS predict the same critical wave number. However, Ooshida's equation under predicts the critical wave number for values of $1/\mathrm{We}$

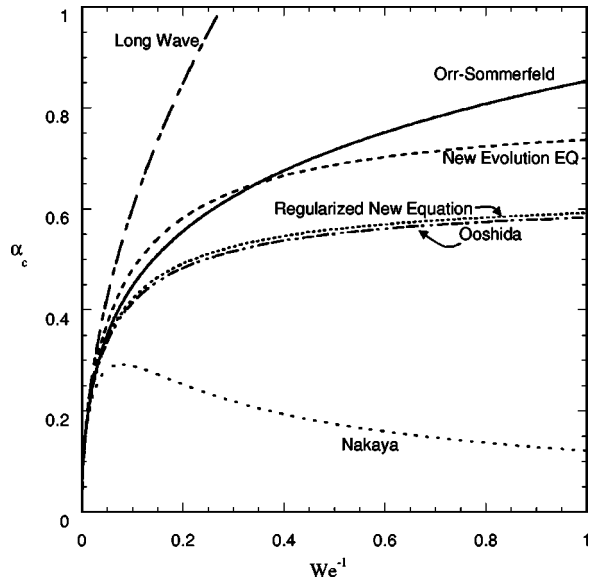

FIG. 6. Neutral stability curves for Ka=10.

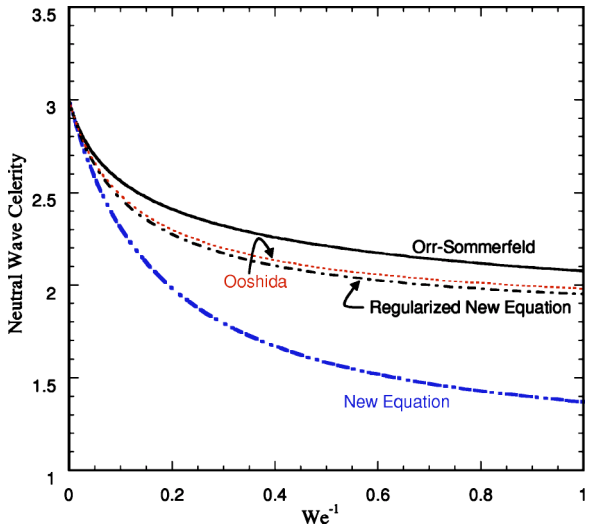

FIG. 7. Critical celerity curves for Ka=10.

away from zero. This overstabilizing effect in Ooshida's equation is due to replacing the spatial derivatives in the viscous and pressure correction terms with time derivative during the regularization procedure. The viscous and pressure correction terms do not have time derivatives in the regular long-wavelength expansion. The neutral stability curves predicted by Eq. (44) are the same as the LW equation though the celerities predicted by it are different from that of the LW equation. Figure 7 shows the critical celerity plots predicted by our equation, its regularized version and other equations.

VII. LOCAL BIFURCATION ANALYSIS

Linear stability results show that the evolution equation (43) is better than the existing single evolution equations in the viscocapillary regime and preserves the qualitative features outside this region. In this section, we present results of local nonlinear analysis on Eq. (43) in the traveling wave coordinate system. We study the waves that travel with a constant shape and velocity, in a coordinate system moving with the wave velocity (Ce). Though the case considered here is an idealization of what is observed, it still gives useful information on the wave structure and maximum wave amplitudes that could be attained, especially for Kapitza numbers of order unity (viscous films). Introducing the steady traveling wave coordinate changes $z=x-\mathrm{Ce}\,t$, $\partial/\partial x=\partial/\partial z$, $\partial/\partial t=-\mathrm{Ce}\,\partial/\partial z$, Eq. (43) can be reduced (after integrating once) to a set of three ordinary differential equations given by

$$\frac{dh_1}{dz} = h_2,$$

$$\frac{dh_2}{dz} = h_3,$$

$$\frac{dh_3}{dz} = -\frac{12\,\mathrm{Ca}}{h_1^3}(\mathrm{Ce} - \mathrm{Ce}\,h_1 + h_1^3 - 1 + 3h_1^4 h_3 + 7h_1^3 h_2^2) - \frac{15}{8\,\mathrm{We}}\mathrm{Ce}\,h_1 h_2 + \frac{81}{40\,\mathrm{We}} h_1^3 h_2, \tag{57}$$

where $(h_1, h_2, h_3)=(h, h_z, h_{zz})$ and Ca(=1/Re We) is the capillary number. The dynamics of the vector field (57) can be studied by integrating the ordinary differential equations numerically for given values of Reynolds and Kapitza numbers, varying the value of celerity (Ce). Asymptotic solutions to Eqs. (57) represent wave forms traveling with constant shape and velocity. Possible solutions include fixed points, periodic wave forms, and trajectories connecting fixed points (homoclinic and heteroclinic orbits). A physical interpretation of each of these solutions can be found in Pumir *et al.* [16] and Chang [17]. The fixed points of the system can be obtained by setting the derivatives on the left-hand side of Eqs. (57) to zero and are given by Eqs. (58) and (59),

$$h_{ss1} = 1, \tag{58}$$

$$h_{ss2} = -\frac{1}{2} + \sqrt{\mathrm{Ce} - \frac{3}{4}}. \tag{59}$$

The first fixed point (58) is the Nusselt's flat film solution and the second fixed point corresponds to the substrate film thickness. The two steady states intersect at Ce=3 and the system undergoes a transcritical bifurcation at this point. The flat film solution is stable for celerity values less than 3 and unstable for celerity above 3. For a given set of parameters

(Ce, We, Ca), information on the stationary solutions other than the fixed points to the vector field near the flat film solution can be obtained by evaluating the eigenvalues of the linear part of the vector field,

$$\mathbf{L} = \begin{pmatrix} 0 & 1 & 0 \\ 0 & 0 & 1 \\ -12(3-\mathrm{Ce})\mathrm{Ca} & -\dfrac{36}{10\,\mathrm{We}} + \dfrac{60}{32}\dfrac{(3-\mathrm{Ce})}{\mathrm{We}} & -36\,\mathrm{Ca} \end{pmatrix}.$$

When all the eigenvalues are negative the flat film solution is stable. If one of eigenvalues is positive, the flat film solution becomes unstable. The matrix **L** has a pair of imaginary eigenvalues (Hopf bifurcation) and a negative eigenvalue when the value of celerity is equal to

$$\mathrm{Ce}_{\mathrm{Hopf}} = \left(\frac{3\,\mathrm{We} + \dfrac{243}{40}}{\mathrm{We} + \dfrac{45}{8}} \right).$$

For $3 < \mathrm{Ce} < \mathrm{Ce}_{\mathrm{Hopf}}$, the flat film is stable, while for $\mathrm{Ce} < \mathrm{Ce}_{\mathrm{Hopf}}$, periodic wave forms emerge from the flat film solution.

Near the point $1/\mathrm{We} \to 0$ and $\mathrm{Ce} \to 3$ in the parameter space, the linear part of the vector field **L** is singular and has two zero eigenvalues and a negative eigenvalue. A Taylor series expansion of Eq. (57) up to second order around the flat film solution $(h_1, h_2, h_3) = (1, 0, 0)$ gives

$$\begin{pmatrix} \dot{H}_1 \\ \dot{H}_2 \\ \dot{H}_3 \end{pmatrix} = \mathbf{L} \begin{pmatrix} H_1 \\ H_2 \\ H_3 \end{pmatrix} + \mathbf{Q}(H_1, H_2, H_3) + \text{higher-order terms},$$

$$\mathbf{L} = \begin{pmatrix} 0 & 1 & 0 \\ 0 & 0 & 1 \\ -12\,\mu\,\mathrm{Ca} & -\dfrac{36}{10}\xi + \dfrac{60}{32}\xi\mu & -36\,\mathrm{Ca} \end{pmatrix}$$

$$\mathbf{Q}(H_1, H_2, H_3) = 36\,\mathrm{Ca}\,H_1^2(\mu - 1) - 84\,\mathrm{Ca}\,H_2^2 + \frac{9}{20}\xi H_1 H_2 + \frac{15}{8}\mu\xi H_1 H_2 - 36\,\mathrm{Ca}\,H_1 H_3, \tag{60}$$

where $\mathrm{H}_1 = \mathrm{H} = h - 1$, $(H_2, H_3) = (H_z, H_{zz})$, $\xi = 1/\mathrm{We}$ and $\mu = 3 - \mathrm{Ce}$ are the deviation variables (small parameters). The linear and quadratic components of the vector field are given by **L** and **Q**, respectively. For a given set of parameters (ξ, μ, Ca), when both the parameters ξ and μ decrease to zero the linear part of the vector field **L** has two zero eigenvalues and a negative eigenvalue. In the three dimensional (3D) phase space (H_1, H_2, H_3) we have a 2D center manifold and a 1D stable manifold spanned by the eigenvectors corresponding to the zero eigenvalues and negative eigenvalue, respectively. Since the flow on a stable manifold rapidly contracts towards the origin, the long term dynamics of the system near the origin can be understood by studying the flow on the center manifold where the solutions can either contract or expand. We use center manifold theorem to reduce the dynamics in the neighborhood of the origin $(H_1, H_2, H_3, \xi, \mu) = (0, 0, 0, 0, 0)$ to the two dimensional center manifold. The above reduction preserves all the qualitative information of Eqs. (60). The dynamics on the center manifold is described by

$$\dot{H}_1 = H_2,$$

$$\dot{H}_2 = -H_1^2 + \frac{1}{18\,\mathrm{Ca}} H_1 H_2 - \frac{\mu}{3} H_1 + \left(\frac{1}{108\,\mathrm{Ca}}\mu - \frac{1}{10\,\mathrm{Ca}}\xi \right) H_2 - \left(\frac{1}{648\,\mathrm{Ca}^2} + \frac{7}{3} \right) H_2^2, \tag{61}$$

where Ca is assumed to be an $O(1)$ parameter. The flow on the center manifold is similar to that obtained by Nguyen and Balakotaiah [7] (using a three equation model) and shows similar bifurcation features. For a detailed account on the local bifurcation analysis we refer the reader to Nguyen and Balakotaiah [7]. Here we present only the main results of the analysis.

The two fixed points $(H_1, H_2) = (0, 0)$ and $(-\mu/3, 0)$ of the system (61) correspond to the flat film solution and substrate film thickness near $\mathrm{Ce} \to 3$. It could be observed by evaluating the eigenvalues of the Jacobian matrix **J** [Eq. (62)] that the stability of the solutions is preserved after center manifold reduction. The steady state corresponding to the flat film solution is stable (sink) for $\mu > 0$ and the substrate film thickness is unstable (saddle node) for all $\mu > 0$. The steady states exchange their stabilities for $\mu < 0$. The Jacobian matrix

$$\mathbf{J} = \begin{pmatrix} 0 & 1 \\ -2H_1 + \dfrac{1}{18\,\mathrm{Ca}} H_2 - \dfrac{\mu}{3} & \dfrac{1}{18\,\mathrm{Ca}} H_1 + \left(\dfrac{1}{108\,\mathrm{Ca}}\mu - \dfrac{1}{10\,\mathrm{Ca}}\xi \right) - 2\left(\dfrac{1}{648\,\mathrm{Ca}^2} + \dfrac{7}{3} \right) H_2 \end{pmatrix} \tag{62}$$

has purely imaginary eigenvalues (Hopf bifurcation) when μ is equal to

$$\mu_h = \frac{108}{10\,\mathrm{We}}. \tag{63}$$

For values of μ above μ_h, asymptotic solutions to Eqs. (61) are given by steady traveling periodic wave forms. The amplitude of these periodic wave forms depends on the value of μ. The Hopf bifurcation is found to be supercritical. An important global bifurcation that can be studied near the double zero singularity is the homoclinic bifurcation which corresponds to a solitary wave. In a homoclinic bifurcation trajectories leaving the steady state along the unstable manifold, return back to the steady state along the stable manifold. Using Melnikov's analysis for homoclinic orbits we obtain analytical correlations (64) and (65) for maximum wave amplitude and celerity of the solitary waves, respectively:

$$h_{max} - 1 = \frac{(3 - \mathrm{Ce})}{6} = \frac{63}{25\,\mathrm{We}} = \frac{2.52}{\mathrm{We}}, \tag{64}$$

$$(3 - \mathrm{Ce}) = \frac{378}{25\,\mathrm{We}} = \frac{15.12}{\mathrm{We}}. \tag{65}$$

It should be noticed that the above correlations depend on the Weber number but not on the Reynolds number. Due to additional assumptions made near double zero singularity, the above relations are valid only in a narrow parameter region where $1/\mathrm{We} \to 0$ and $\mathrm{Ca} \sim O(1)$. However, the full model [Eqs. (57)] has a much larger region of validity and could be used to study numerically the wave structure and maximum wave amplitudes.

Validity of Eq. (43)

The first and second order long-wavelength equations show finite time blowup [15,16,20,21]. Pumir *et al.* [16] showed that such a behavior can be related to the homoclinic celerity vs Reynolds number diagram, which in case of long-wavelength equation shows saddle-node bifurcation. The curve turns back at $\mathrm{Re} \approx 3.97$ ($\mathrm{Ka} = 252$). It was argued that such a turn back signals finite time blowup.

Owing to the nature of its eigenvalues, Eq. (43) shows the following bifurcation picture for both the higher ($\mathrm{Ce} \geqslant 3$) and lower celerity ($\mathrm{Ce} \leqslant 3$) branches. For a fixed Ka and Re, as one varies the celerity from 3 to a higher/lower value, the stable state undergoes Hopf bifurcation. On further varying the celerity we reach the homoclinic point. The $\mathrm{Ce_{Hopf}}$ and $\mathrm{Ce_{hom}}$ trends are the same, i.e., if the $\mathrm{Ce_{hom}}$ vs Re diagram shows a turn back, so does the $\mathrm{Ce_{Hopf}}$ vs Re diagram. Thus, instead of calculating $\mathrm{Ce_{hom}}$, we would do well to just find how $\mathrm{Ce_{Hopf}}$ changes with changes in flow rate both for the higher and lower branches.

Equation (43) gives the following expressions for $\mathrm{Ce_{Hopf}}$:

$$\mathrm{We} = \frac{9(25\ \mathrm{Ce_{Hopf}}\ h_0^6 - 27\ h_0^8)}{40(3 - 3\ \mathrm{Ce_{Hopf}} + 2\ \mathrm{Ce_{Hopf}}\ h_0)}, \tag{66}$$

where

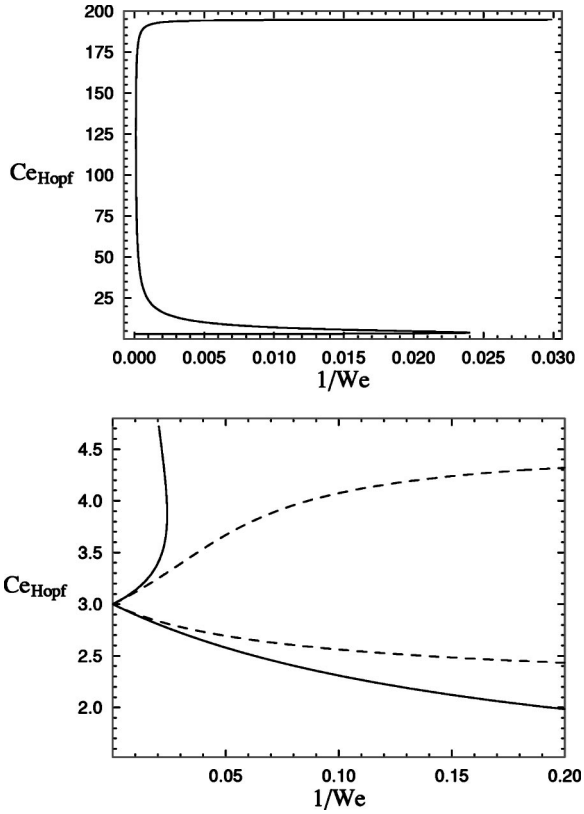

FIG. 8. Top: The Hopf celerity $\mathrm{Ce_{Hopf}}$ as a function of the Weber number We, given by Eq. (43). Only plot for the branch with celerity greater than 3 is shown. Bottom: The Hopf celerity $\mathrm{Ce_{Hopf}}$ vs Weber number We curves. Solid curve corresponds to Eq. (43) and the dashed curve is that given by Ooshida's equation. Both branches with celerities greater than and less than 3 are shown.

$$h_0 = \begin{cases} h_{ss1} \text{ if } \mathrm{Ce} \leqslant 3, \\ h_{ss2} \text{ if } \mathrm{Ce} \geqslant 3. \end{cases} \tag{67}$$

The h_{ss2} solution is termed the higher branch and h_{ss1} as the lower branch. Notice that $\mathrm{Ce_{Hopf}}$ depends only on the Weber number. The first plot in Fig. 8 shows $\mathrm{Ce_{Hopf}}$ vs We diagram for the higher branch. The curve turns back and increases to a large value before it plateaus at a constant value. The second plot in Fig. 8 shows $\mathrm{Ce_{Hopf}}$ vs We plots predicted by Eqs. (43) and (47). The diagram shows that for Eq. (43), $\mathrm{Ce_{Hopf}}$ turns back while Ooshida's $\mathrm{Ce_{Hopf}}$ does not, signalling that Eq. (43) is not free from finite time blowup. While Ooshida's equation quells the finite time blowup associated with the long-wavelength equation, our single evolution equation does not discard itself of this shortcoming.

Regularization

One would then be prompted to regularize Eq. (43). Ooshida regularized Gjevik's second order long-wavelength equation. As pointed earlier, time space exchange leads to the long-wavelength equations. In what follows we would selectively regularize Eq. (43), and it would be shown that the regularized equation has acceptable properties.

In Sec. IV, we have assumed that $\tau = \alpha\, t$, which assumes that τ is small. In order that the regularized equation be valid for much longer times, we would have to regularize in time rather than in space. From Eq. (41), flow rate q can be written as

$$q = h^3 - \gamma^{11}\frac{5}{32}\beta\, h^4\, h_t + \gamma^{10}(7\, h^3 h_x{}^2 + 3\, h^4 h_{xx}) + \gamma^{11}\left(\frac{1}{12}\beta\, W\, h^3\, h_{xxx} - \frac{27}{160}\beta\, h^6\, h_x\right) = \overline{q} + \tilde{q}, \quad (68)$$

where $\overline{q}$ and $\tilde{q}$ are defined by

$$\overline{q} = h^3 - \gamma^{11}\frac{5}{32}\beta\, h^4\, h_t = \overline{q_0} + \gamma^{11}\overline{q_{11}} \quad (69)$$

and

$$\tilde{q} = \gamma^{10}(7\, h^3 h_x^2 + 3\, h^4 h_{xx}) + \gamma^{11}\left(\frac{1}{12}\beta\, W\, h^3\, h_{xxx} - \frac{27}{160}\beta\, h^6\, h_x\right). \quad (70)$$

We would want to regularize $\overline{q}$ only. Let

$$\overline{L} = 1 + \gamma^{11} e_1 \beta \partial_t \quad (71)$$

be the operator, then define

$$\overline{S} = \overline{L}\overline{q} = \overline{q_0} + \gamma^{11}(\overline{q_{11}} + e_1\beta\partial_t \overline{q_0}) = \overline{S_0} + \overline{S_{11}}. \quad (72)$$

Following Ooshida, setting $\overline{S_{11}}$ to zero would yield a value for e_1 which can be function of h, thus

$$e_1\beta(3h^2 h_t) - \frac{5}{32}\beta h^4 h_t = 0 \quad (73)$$

or

$$e_1 = \frac{5}{96}h^2 \quad (74)$$

and $\overline{L}$ becomes $\overline{L} = 1 + \gamma^{11}\frac{5}{96}h^2\beta\partial_t$. The regularized equation is obtained by operating $\overline{L}$ on $q = \overline{q} + \tilde{q}$ or

$$\overline{L}q = \overline{L}\overline{q} + \overline{L}\tilde{q} = \overline{S} + \overline{L}\tilde{q} = \overline{S_0} + \overline{L}\tilde{q} \quad (75)$$

and we get

$$q + \gamma^{11}\frac{5}{96}h^2\beta\partial_t q = h^3 + \gamma^{10}(7h^3 h_x{}^2 + 3h^4 h_{xx}) + \gamma^{11}\left(\frac{1}{12}\beta W h^3 h_{xxx}\right) - \gamma^{11}\left(\frac{27}{160}\beta h^6 h_x\right). \quad (76)$$

To close the above equation we require the kinematic boundary condition $h_t + q_x = 0$. The overall equation would then be

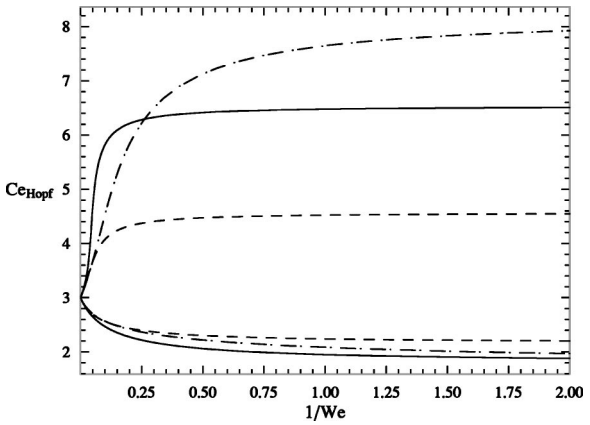

FIG. 9. The Hopf celerity $\mathrm{Ce}_{\mathrm{Hopf}}$ vs Weber number We curves. Solid curve corresponds to our regularized Eq. (77) , the dashed curve is that given by Ooshida's equation and the dot-dashed curve is that given by Ruyer-Quil and Manneville's second order Galerkin model. Both branches with celerities greater than and less than 3 are shown.

$$q + \frac{5}{96}h^2\ \mathrm{Re}\partial_t q = h^3 + 7h^3 h_x^2 + 3h^4 h_{xx} + \frac{1}{12}\mathrm{Re\ We}h^3 h_{xxx} - \frac{27}{160}\mathrm{Re}h^6 h_x. \quad (77)$$

Our regularized equation is accurate up to $O(\gamma^{11})$ and is an equation in flow rate q and surface height h. It appears that one needs at least two modes (h and q) to satisfactorily predict qualitative thin film dynamics as pointed by Ruyer-Quil and Manneville [21].

Temporal linear stability analysis of our regularized equation gives the following expressions for the neutral wave number and neutral celerities:

$$\mathrm{Ce}_c = 3(1 - \alpha_c^2), \quad (78)$$

$$\alpha_c = \frac{\sqrt{45 + 4\ \mathrm{We} - \sqrt{729 + 360\ \mathrm{We} + 16\ \mathrm{We}^2}}}{3\sqrt{5}}. \quad (79)$$

The critical Reynolds number in case of inclined films is predicted to be $\mathrm{Re}_c = \frac{10}{3}\cot(\theta)$. Among the earlier two mode models, only those developed by Ruyer-quil and Manneville [21] predict the right critical Reynolds number which is given above. Our regularized equation has the minimum number of terms neccessary to describe qualitatively accurate dynamics of thin film flows. The equation includes viscous dissipation, surface tension, and inertial terms, all of which are required for accurate predictions.

The $\mathrm{Ce}_{\mathrm{Hopf}}$ predictions of Eq. (77) shown in Fig. 9 are given by the expression

$$\mathrm{We} = \frac{3\ h_0^4(25\ \mathrm{Ce}_{\mathrm{Hopf}}^2 - 81\ h_0^4)}{40(3 - 3\ \mathrm{Ce}_{\mathrm{Hopf}} + 2\ \mathrm{Ce}_{\mathrm{Hopf}}\ h_0)}, \quad (80)$$

where h_0 is given by Eq. (67) . Also shown in the figure are Ooshida [15] 's predictions and $\mathrm{Ce}_{\mathrm{Hopf}}$ predictions of Ruyer-Quil and Manneville's simplified second order Galerkin

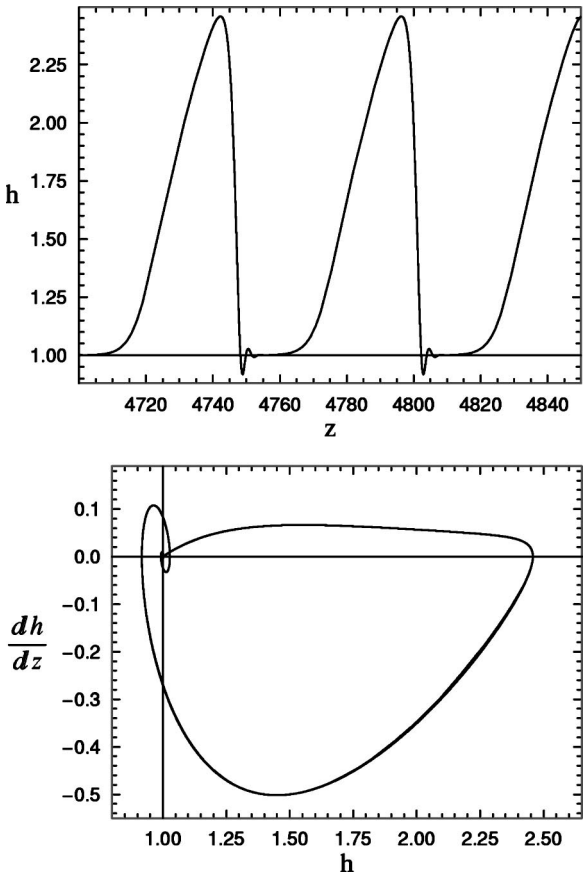

FIG. 10. Homoclinic wave profile and its phase portrait in the steady traveling coordinate predicted by Eq. (77). $Ce_{hom}=6.878\,286, Re=4.0, Ka=6.0, We=8.6535, Ce_{Hopf}=5.9356$.

model. Our regularized equation is free of finite time blowup. Linear stability and Hopf analysis indicate that our regularized equation over stabilizes the system, the Hopf celerity predictions are off by a factor of 1.3 as compared to those predicted Ruyer-Quil and Manneville [21], while Ooshida's predictions are off by a factor of 2. Shakadov's model given by Eq. (3) does not show Hopf bifurcation, however, it predicts homoclinic celerities as high as 7.67 (see Table 8.1 and Fig. 3.5 of Chang and Demekhin [5]).

Equation (61) obtained by center manifold reduction remains the same for the higher and lower branch, for the alternative equation and its regularized version. Equations (64) and (65) now read, $H_{1max}=2.52/We$ and $\pm(Ce-3)=15.12/We$, H_1 being the deviation from steady state (the higher branch is approximated by $h_{ss2}=1+\mu/3-\mu^2/27$, where $\mu=Ce-3$). Figure 10 shows a homoclinic wave profile and its phase portrait predicted by the new regularized equation. Various other homoclinic profiles are shown in Fig. 11, for different Ka and Re. Notice that Ce_{hom} is an extract of global bifurcation and depends on the Kapitza and Reynolds numbers (see Figs. 10 and 11) unlike Ce_{Hopf} which only depends on the Weber number. However, Ce_{hom} is never less (greater) than Ce_{Hopf} for the higher (lower) branch. The higher branch homoclinic celerity predictions of Eq. (77) for $Ka=1$ are shown in Fig. 12, also shown in the figure are the corresponding homoclinic celerities of single hump solitary

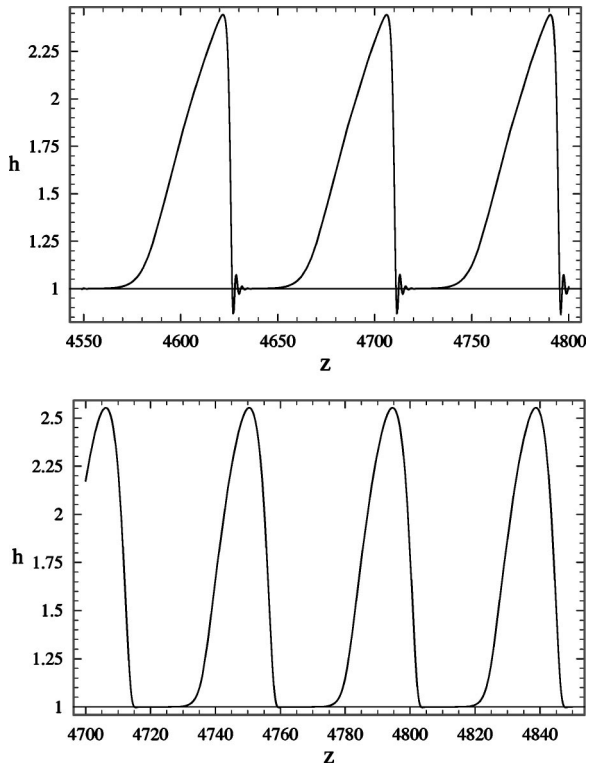

FIG. 11. Homoclinic wave profiles in the steady traveling coordinate-predicted by Eq. (77). Top: $Ce_{hom}=6.667\,53, Re=7.0, Ka=10.0, We=5.6751$. Bottom: $Ce_{hom}=7.447\,965, Re=1.3651, Ka=1.0, We=8.6535$.

waves predicted by Ruyer-Quil and Manneville's second order Galerkin model. Lines through the data points are cubic spline fits of the respective data.

VIII. NUMERICAL RESULTS ON WAVE AMPLITUDES AND COMPARISON WITH EXPERIMENTAL DATA

In this section numerical simulation results of our evolution equation (43) in the traveling wave coordinate are presented. The results are compared to those of Eq. (44) . The predictions of the two equations are found to be significantly different. The system given by Eq. (57) has three independent parameters Re, Ka, and Ce. The equations are integrated for fixed values of Re and Ka, varying the value of celerity (Ce). A slight perturbation of the flat film solution is used as the initial condition. Celerity values are explored in the range $Ce_{hom}<Ce<3$, where Ce_{hom} is the value of celerity at homoclinic point. Beyond Ce_{hom} the system does not have a solution, i.e., there are no wave forms traveling with constant shape at celerities lower than Ce_{hom}. For given values of Re and Ka, the flat film solution is found to be stable in the celerity range $Ce_{Hopf}<Ce<3$, where Ce_{Hopf} is the celerity at Hopf bifurcation. When the value of celerity is reduced below Ce_{Hopf}, periodic wave forms were observed. The amplitude and time period of these waves were found to increase for values of celerity away from Ce_{Hopf}. Upon decreasing the celerity further ($Ce_{hom}<Ce<Ce_{Hopf}$), the evolution of wave

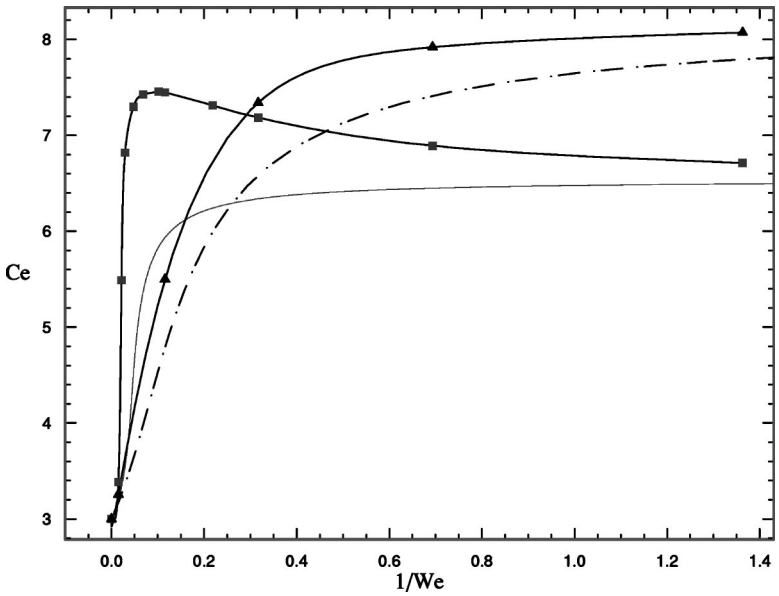

FIG. 12. Plot of homoclinic and Hopf celerities for Ka=1. The solid line and squares are Hopf and homoclinic celerities given by Eq. (77). The dot-dashed line and triangles are Hopf and homoclinic celerities predicted by Ruyer-Quil and Manneville's second order Galerkin model. Lines running through the data points are cubic spline fits of respective data.

structure from periodic to more complex wave profiles (period 2, period 4,…, chaotic, and homoclinic) is found to depend greatly on the Kapitza number. In the remaining part of this section we discuss the transition of wave structure from periodic to homoclinic orbit for different values of the Kapitza number, and compare the maximum wave amplitudes obtained with experimental data.

Numerical simulations show that the wave structure is more regular (periodic or quasiperiodic) at low Kapitza numbers where viscous effects are predominant over inertial effects. *The route from periodic to homoclinic orbit consists only of period-1 solutions for small Kapitza numbers*. As the value of celerity is reduced from Ce_{Hopf} to Ce_{hom}, the amplitude and time period of the waves increases. The time period of the waves near the homoclinic orbit is much higher than the time period of the periodic solutions (at the homoclinic point, the time period is infinity and we obtain a solitary wave). Complex wave structure (chaotic solutions) is not observed in this case even up to Weber numbers of the order unity or $Re \sim Ka^{3/5}$. Figure 13 shows bifurcation diagrams of film thickness versus Ce for Ka=1.0 and Reynolds numbers Re=0.5 and Re=1.0, computed using Eq. (57). Periodic

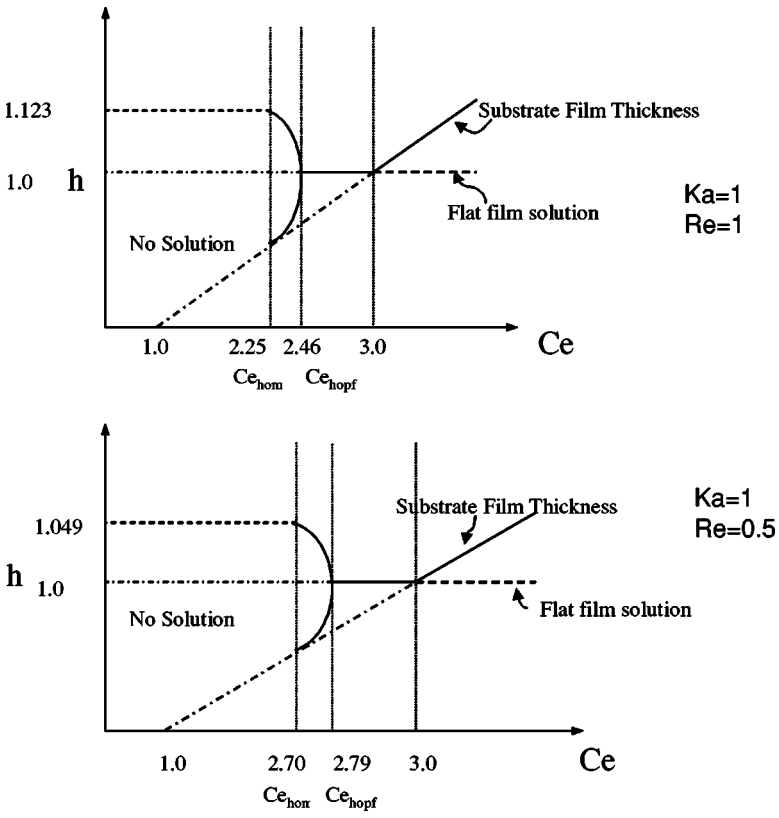

FIG. 13. Top: Bifurcation diagram of film thickness versus celerity for Ka=1 and Re=1. Bottom: Bifurcation diagram of film thickness versus celerity for Ka=1 and Re=0.5.

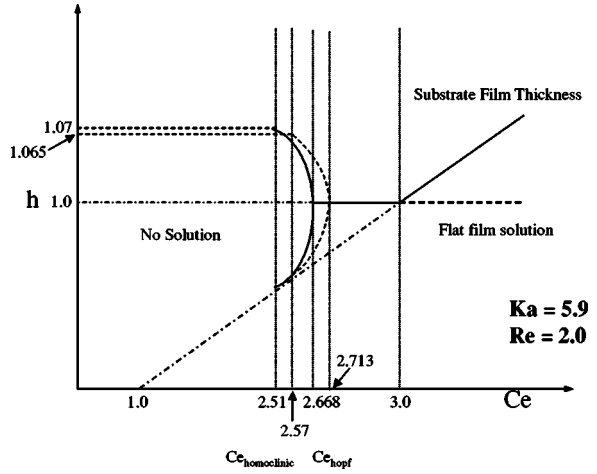

FIG. 14. Bifurcation diagram of film thickness versus celerity for Ka=5.9 and Re=2.0. Values indicated with the arrows are those given by the regularized equation (77).

wave forms originate from the flat film steady state for values of celerity less than Ce_{Hopf}. The amplitude of these waves increases until it touches the substrate film thickness at Ce_{hom}. Period doubling is not observed for both Re=0.5 and Re=1.0. Same is the case for Ka=5.9 and Re=2.0 (Fig. 14). Also shown in Fig. 14 is the bifurcation diagram predicted by our regularized equation (77). Only steady periodic wave forms are observed. For intermediate values of Kapitza number the transition from periodic to homoclinic orbit consists of period-2 and period-4 solutions up to Reynolds number of the order $Ka^{3/5}$. Figure 15 shows the bifurcation diagram of *h* vs Ce for Ka=10.0. Period doubling is observed for Ka=10.0 and Reynolds numbers 2.0 and 5.0. Whereas (in Fig. 16) for a Reynolds number of 2.1 and Ka=13.0 period-2 and period-4 solutions are observed. For higher values of the Kapitza number, it is found that the transition consists of period-2, period-4, and chaotic solutions before reaching the homoclinic orbit. This is shown in Fig. 16 for Ka=22.0 and Re=5.4. The above observations suggest that the *waves are more regular at low Kapitza numbers and the complexity of wave structure increases with increasing Kapitza number even at low Reynolds numbers. Hence the interface is very dynamic and can exhibit spatiotemporal chaos at low Reynolds numbers for large values of the Kapitza number*. Experimental wave traces measured in our laboratory [18] for Ka=5.9, Re=2.0 and Ka=13, Re=2.1 are shown in Figs. 17(b) and 18(b), respectively. It could be seen from these wave traces that waves are more regular at low Kapitza number for the same Reynolds number. In Figs. 17 and 18, experimental wave traces are compared to numerically simulated wave profiles for Ka=5.9, Re=2.0 and Ka=13, Re=2.1.

A comparison of experimental data [7] with numerical simulation results for maximum wave amplitudes in the viscocapillary regime ($We>1$ or $Re<Ka^{3/5}$) is shown in Fig. 19. The plot shows that the model results are in good agreement with experimental data in the viscocapillary regime. However, the model underpredicts the maximum wave amplitudes outside the viscocapillary regime and for high values of the Kapitza number. This is because the waves outside the viscocapillary regime and for high Ka are multipeaked (chaotic wave structure). Since the wave celerity depends on

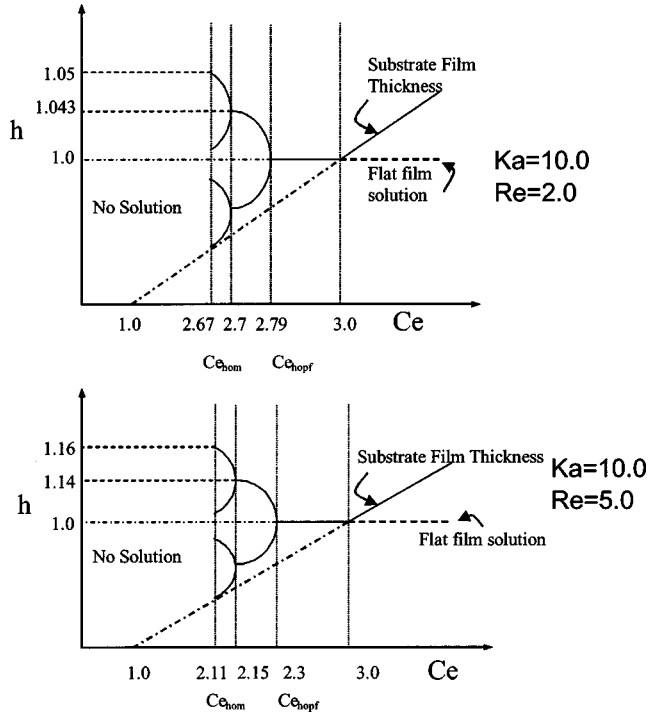

FIG. 15. Top: Bifurcation diagram of film thickness versus celerity for Ka=10 and Re=2.0. Bottom: Bifurcation diagram of film thickness versus celerity for Ka=10 and Re=5.0.

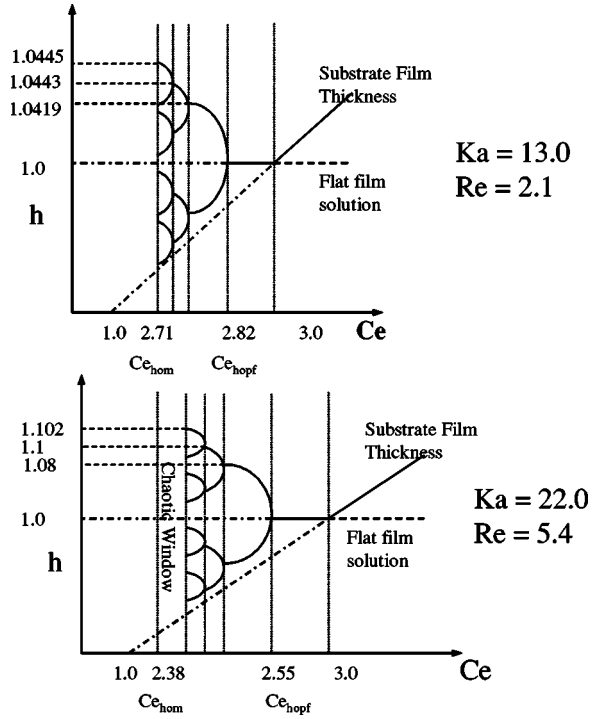

FIG. 16. Top: Bifurcation diagram of film thickness versus celerity for Ka=13 and Re=2.1. Bottom: Bifurcation diagram of film thickness versus celerity for Ka=22 and Re=5.4.

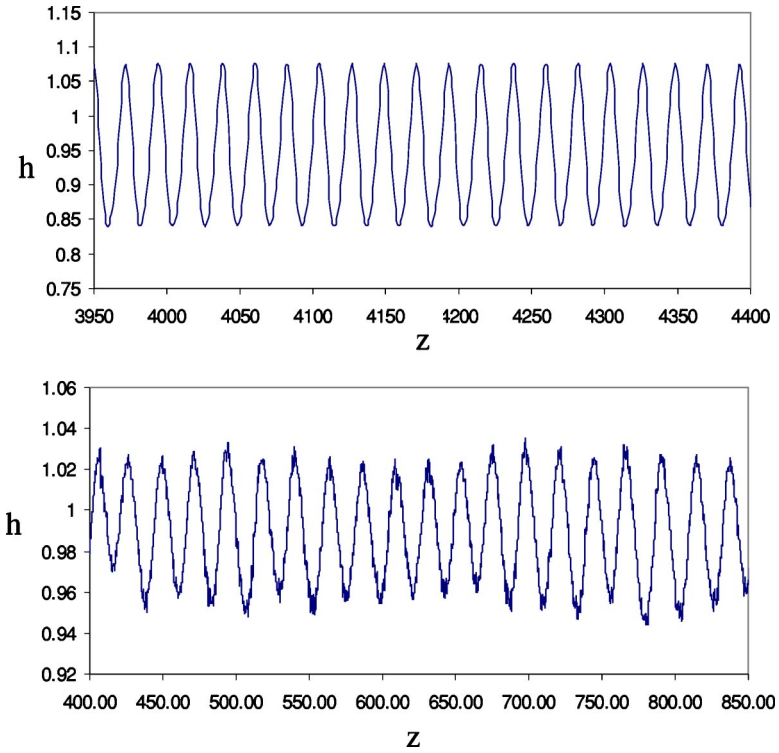

FIG. 17. Top: Numerical wave traces obtained from Eq. (43) for Ka=5.9 and Re=2.0. Bottom: Experimental wave traces for Ka=5.9 and Re =2.0.

the wave amplitude, the probability of wave merging and splitting increases when the waves are multipeaked. These phenomena (merging and splitting of waves) cannot be accounted for in the traveling wave coordinate system and hence the wave amplitudes are under predicted in the traveling wave coordinate for Weber numbers outside the viscocapillary regime and for high values of the Kapitza number. The traveling wave analysis cannot be used to explain experimental data once the wave structure becomes nonperiodic.

Figure 20 shows the plot of maximum wave amplitude versus 1/We for Ka=13 computed using the new equation.

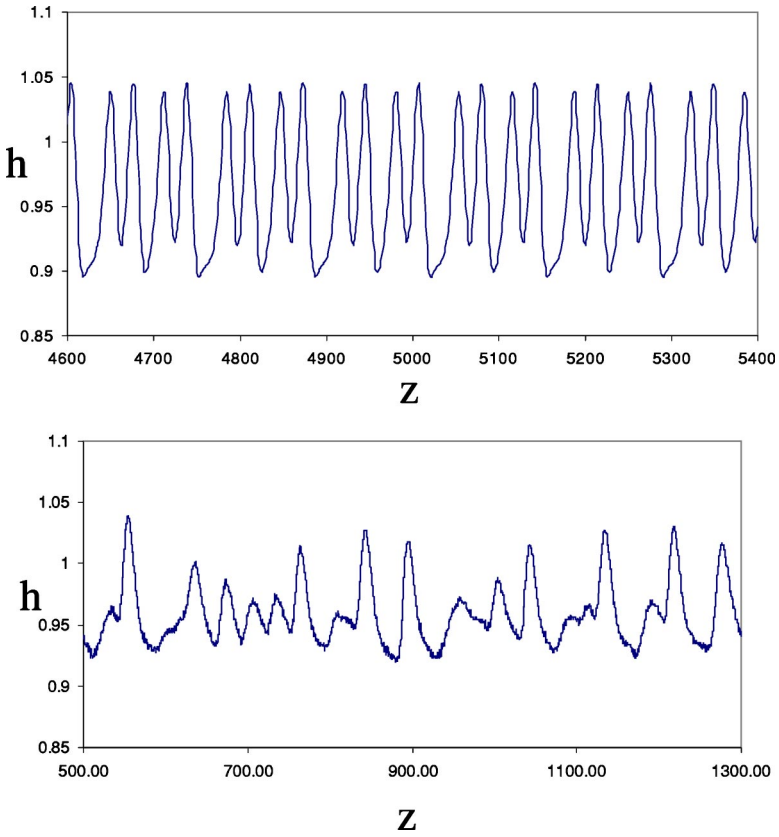

FIG. 18. Top: Numerical wave traces obtained from Eq. (43) for Ka=13 and Re=2.1. Bottom: Experimental wave traces for Ka=13.0 and Re =2.1.

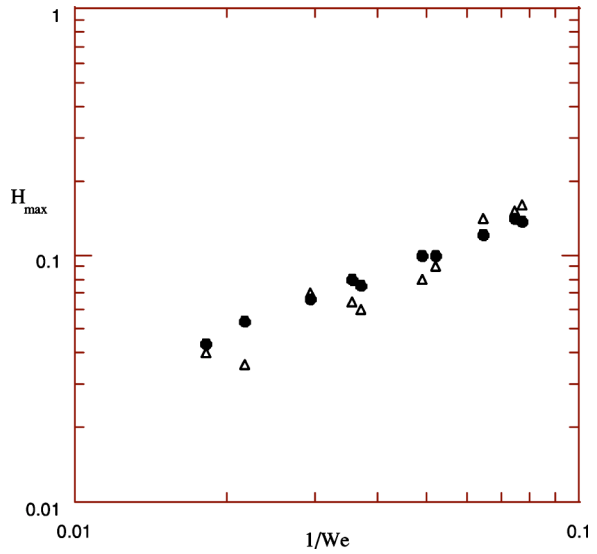

FIG. 19. Comparison of experimental and numerical simulation results on maximum wave amplitudes. The triangles denote experimental data and the dots are numerical simulations from Eq. (43).

The plot shows that the double zero scaling is good near $1/\mathrm{We}\rightarrow 0$. The wave amplitudes are found to increase rapidly in the viscocapillary regime ($\mathrm{We}\gg 1$) with increasing $1/\mathrm{We}$ or Reynolds number. But for Weber numbers $\mathrm{We}\sim O(1)$ the increase in wave amplitudes becomes gradual. For $\mathrm{We}<1$ the wave amplitudes are found to decrease. Following this observation, we have recently conducted experiments on vertically falling films in the viscous regime ($53<\mathrm{Ka}<693$). In these experiments, the pipe diameter and fluid physical properties (Ka number) were fixed, the flow rate (Re) was varied, and the maximum wave amplitude was determined as a function of Re. It was found that the wave amplitude initially increased with flow rate, reached a maximum (around We values of order unity) and then decreased.

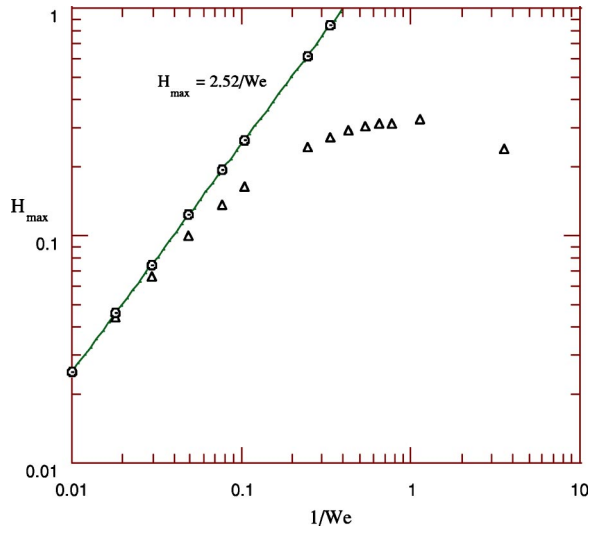

FIG. 20. Maximum film thickness versus $1/\mathrm{We}$ for $\mathrm{Ka}=13.0$. The triangles denote the numerically determined maximum film thickness while the circles (and the line) denote the scaling near the double zero eigenvalue obtained from local bifurcation analysis.

This behavior, observed only for some range of fluid viscosities, is in qualitative agreement with the model predictions. These experimental results on wave suppression will be published separately. It should be noted here that the assumption $\mathrm{We}\gg 1$ for which the model is derived fails in the inertial regime and hence the model predictions are quantitatively off. However, the model shows correct qualitative features.

Equation (44), obtained by replacing the time derivative in Eq. (43) with a spatial derivative is also integrated in the traveling wave coordinate. Comparison of the maximum wave amplitudes predicted by Eq. (44) to experimental data shows that it overpredicts the wave amplitudes in the viscocapillary regime ($\mathrm{Re}<\mathrm{Ka}^{3/5}$). More important, Eq. (44) predicts nonphysical wave celerities for Reynolds number of the order $\mathrm{Re}\sim\mathrm{Ka}^{3/5}$. The phenomenon of wave suppression in the inertial regime which is captured qualitatively by Eq. (43) is not predicted by Eq. (44) . The $O(\gamma^{21})$ and higher order terms neglected in Eq. (44) while exchanging time derivative with spatial derivative become important at Weber numbers of order unity. Since the h_{xt} term in Eq. (43) retains all these neglected terms, it predicts the wave suppression qualitatively. The inertial effects are not completely accounted for in Eq. (44) when the time derivative which is present in the inertial term is replaced with a spatial derivative that comes from viscous contribution. Based on the linear stability results and traveling wave analysis it could be seen that Eq. (43) is a better model than Eq. (44) for describing wave evolution on viscous films. Integrating the model [Eq. (43)], neglecting the viscous and pressure correction term $7h^3h_x^2$ shows that the maximum wave amplitudes are over predicted and the solution diverges even in the viscocapillary regime. Hence the nonlinear term $7h^3h_x^2$ acts as a growth arresting term and cannot be neglected.

IX. CONCLUSIONS

In this work, the scaling, $\mathrm{Ka}\sim O(1)$ and $\alpha^2\mathrm{We}\sim O(1)$, is presented to develop low-dimensional models for vertically falling viscous films. Using the scaling proposed, an alternative evolution equation and its regularized version are derived for describing waves on the surface of a falling film in the viscocapillary regime ($\mathrm{We}\gg 1$ or $0<\mathrm{Re}\ll 5\ \mathrm{Ka}^{3/5}$). The alternative equations include viscous dissipation and pressure correction terms that are missing in the existing single evolution equations. In particular, we have shown that both $3h^4h_{xx}$ and $7h^3h_x^2$ terms are necessary for quantitative description of wave amplitudes in the viscocapillary regime. The exchange between time and space derivatives which was used in earlier models is shown to be inaccurate. Though replacing time with a spatial derivative recasts the evolution equation into a form conducive for analytical and numerical analysis, it changes the predictions of the equation both qualitatively and quantitatively. It should be emphasized that for falling films, *it is the magnitude of the Weber number that determines the viscous and inertia dominated regimes, and not the Reynolds number*.

An important outcome of numerical studies of the new equations is that the wave structure is not always chaotic but becomes regular for low Kapitza numbers in the viscocapil-

lary regime. For a fixed Reynolds number, the wave structure becomes more and more complex as the Kapitza number is increased. The regular structure exhibited by the waves at low Kapitza numbers could be used to understand wavy film flow in more complex geometries. This model also predicts qualitatively suppression of waves for values of Weber number around unity.

ACKNOWLEDGMENT

This work was partially supported by a grant from the Institute for Space Systems Operations at University of Houston.

APPENDIX A: EVOLUTION EQUATION FOR 3D FILM FLOWS

The 3D version of Eq. (43) can be derived and is given by

$$h_t + 3h^2h_x + \frac{\partial}{\partial x}\left[3h^4h_{xx} + 7h^3h_x^2 + \frac{3}{2}h^3h_z^2 + \frac{5}{8}h^4h_{zz} - \frac{5}{32}\mathrm{Re}h^4h_t - \frac{27}{160}\mathrm{Re}h^6h_x\right] + \frac{\partial}{\partial x}\left[\frac{\mathrm{Re\ We}}{12}(h^3h_{xzz} + h^3h_{xxx})\right] + \frac{\partial}{\partial z}\left[\frac{11}{2}h^3h_zh_x + \frac{19}{8}h^4h_{xz} + \frac{\mathrm{Re\ We}}{12}(h^3h_{xxz} + h^3h_{zzz})\right] = 0.$$

This equation may be compared to the evolution equation for three dimensional waves that was derived by Atherton and Homsy [19] using the traditional long-wavelength scaling [$\mathrm{Re} \sim O(1)$ and $\alpha^2\ \mathrm{We} \sim O(1)$]. To order α, the three dimensional long-wavelength equation is

$$h_t + 3h^2h_x + \frac{\partial}{\partial x}\left[\frac{3}{10}\mathrm{Re}h^6h_x + \frac{\mathrm{Re\ We}}{12}(h^3h_{xxx} + h^3h_{xzz})\right] + \frac{\partial}{\partial z}\left[\frac{\mathrm{Re\ We}}{12}(h^3h_{zzz} + h^3h_{zxx})\right] = 0.$$

As mentioned earlier, in this scaling the missing viscous and pressure correction terms appear at higher orders.

APPENDIX B: SMALL-AMPLITUDE EXPANSION

A small-amplitude expansion of Eq. (43) can be derived and leads to an equation of the form

$$\eta_T + \eta\eta_X + \delta_1\eta_{XXX} - \delta_2\eta_{TX} + \eta_{XX} + \eta_{XXXX} = 0,$$

where $\delta_1 = 3.807\ \mathrm{We}^{1/10}/\mathrm{Ka}^{3/5}$ and $\delta_2 = 1.477\ \mathrm{Ka}^{3/5}/\mathrm{We}^{11/10}$. Further details and comparison with the Kuromoto-Sivashinsky equation can be found in Panga and Balakotaiah [11].

[1] W. Nusselt, Z. Ver. Deut. Ing. 60, 541 (1916).
[2] P. L. Kapitza and S. P. Kapitza, Zh. Eksp. Teor. Fiz. **19**, 105 (1949).
[3] T. B. Benjamin, J. Fluid Mech. **2**, 554 (1957).
[4] H. C. Chang, Annu. Rev. Fluid Mech. **26**, 103 (1994).
[5] H. C. Chang and E. A. Demekhin, *Complex Wave Dynamics on Thin Films* (Elsevier Scientific, New York, 2002).
[6] D. J. Benney, J. Math. Phys. **45**, 150 (1966).
[7] L. T. Nguyen and V. Balakotaiah, Phys. Fluids **12**, 2236 (2000).
[8] B. Gjevik, Phys. Fluids **13**, 1918 (1970).
[9] C. Nakaya, Phys. Fluids **18**, 1407 (1975).
[10] C. Ruyer-Quil and P. Manneville, Eur. Phys. J. B **6**, 277 (1998).
[11] M. K. R. Panga and V. Balakotaiah, Phys. Rev. Lett. **90**, 154501 (2003).
[12] P. Aussillous and D. Quéré, Phys. Fluids **12**, 2367 (2000).
[13] T. B. Benjamin, J. L. Bona, and J. J. Mahony, Philos. Trans. R. Soc. London, Ser. A **272**, 47 (1972).
[14] A. L. Frenkel and K. Indireshkumar, Phys. Rev. E **60**, 4143 (1999).
[15] T. Ooshida, Phys. Fluids **11**, 3247 (1999).
[16] A. Pumir, A. Manneville, and Y. Pomeau, J. Fluid Mech. **135**, 27 (1983).
[17] H. C. Chang, Phys. Fluids A **1**, 1314 (1989).
[18] L. T. Nguyen, Ph.D. thesis, University of Houston, 1999.
[19] R. W. Atherton and G. M. Homsy, Chem. Eng. Commun. **2**, 57 (1976).
[20] S. W. Joo, S. H. Davis, and S. G. Bankoff, Phys. Fluids A **3**, 231 (1991).
[21] C. Ruyer-Quil and P. Manneville, Eur. Phys. J. B **15**, 357 (2000).